

# Temporal Broadening of Attosecond Pulse Trains Induced by Multi-Band inference in Solid-State High-Order Harmonic Generation

Qing-Guo Fan<sup>1,2</sup>, Kang Lai<sup>1</sup>, Wen-hao Liu<sup>1</sup>, Zhi Wang<sup>1</sup>, Lin-Wang Wang<sup>1,2</sup>, Jun-Wei Luo<sup>1,2</sup>

<sup>1</sup> State Key Laboratory of Semiconductor Physics and Chip Technologies, Institute of Semiconductors, Chinese Academy of Sciences, Beijing 100083, China

<sup>2</sup> Center of Material Science and Optoelectronics Engineering, University of Chinese Academy of Sciences, Beijing 100049, China

**Abstract:** The mechanism underlying high harmonic generation (HHG) in gases has been well clarified, characterizing attosecond pulse trains (APT) in the time domain, significantly advances the synthesis of isolated attosecond pulse (IAP). However, the complexity of HHG in solid obstacles IAP separation. Here, we use time-dependent density functional theory (TDDFT) to investigate the multiband mechanism of APT in solid state with bulk silicon as prototype. Our research unveils that: 1. The temporal characteristics of APT can be characterized by the occupation of electrons in different energy bands. 2. Due to the temporal occupation difference caused by optical transition allowed (or forbidden) by symmetry between different conduction bands and valence bands, a harmful phase shift in harmonics emission to APT for extracting IAP occurs. Our findings not only shed light on the mechanisms behind solid-state HHG but also provide new avenues to control APT to generate IAP.

## I. INTRODUCTION

The interaction between intense laser fields and atoms or molecules, which leads to emitting photons several times higher than the fundamental laser center frequency, has open the door to attosecond science [1–3]. The elucidation of mechanism in gas-HHG occurred approximately three decades ago [4,5], has facilitated the acquisition of IAP [6,7].

A decade ago, the discovery of non-perturbative solid-state HHG in experiment aroused wide attention [8–17]. Nowadays, the fundamental physical mechanisms have been gradually

clarifying [17,18]. It consists of intra-band and inter-band process, where intra-band mechanism is stemming from classical Bloch oscillation [8,19,20], inter-band mechanism can be viewed as a generalized electron-hole recollision process [20,21] by semi-classical analysis. However, the physical picture of inter-band could be more intricate within complex bandstructure. For example, interference between long and short trajectories leads to the splitting of harmonic peaks [22], multiple plateaus of spectral feature originates from multiple bands [23], spectral caustics occurs at Van Hove singularities [24] and so on. On the other hand, the high electron density [25] and momentum changes induced by the periodic lattice structure [26] of solid material may result in strong HHG spectra. Couple with their controllable nature, solid materials show appealing promise for future solid-state attosecond sources [11]. Challenges remain in using solid-state HHG for attosecond pulse due to material damage thresholds [27] and debated physical mechanisms [13,19–21,28–32]. One of the most critical factors is the impact of multi-band structures in solids on APT. For instance, interference between multiple valence bands can either cancel or enhance certain time intervals of APT, influencing IAP extraction [9], even order harmonics originating from the optical interference the between polarization emission from different pairs of bands [33], spectral splitting results from interference between different emission trajectories [22], angular shifts of parallel-polarized odd harmonics due to the involvement of multiple conduction bands [34].

To tackle these challenges, we employ time-dependent density functional theory (TDDFT) using bulk silicon as prototype and unveil the harmful impact on APT from multi-band emission mechanism in time domain. Our analysis shows that it would broaden the full width at half maximum (FWHM) of APT (Figure 1). We design different laser intensities scenarios and apply low-pass filtering to all signals, with setting the cutoff energy of the lowest light intensity as the upper limit (4.3eV). To conduct a quantitative and specific analysis, we select the maximum peak of the filtered signal as the subject of our study. Our results demonstrate that: With the rising field strength, albeit the maximum peak intensity increases rapidly and monotonically (see **APPENDIX B**), the corresponding center and FWHM of peak exhibit intriguingly non-monotonic variation which implies the presence of complex emission mechanism (Figure 1(d),(e)). Figure

1(b) illustrates it in detail. Initially, the electrons located at valence band maximum ( $\Gamma$  point) are excited to the conduction bands [10] (Figure 1(b), solid red line and arrow, ignoring pre-acceleration process [32] for simplicity), leaving holes in valence bands. Next, electrons and holes accelerate, emitting photons due to the non-parabolic bandstructure. Finally, carriers can emit photons through recombination. Most importantly, there are two possible scenarios for the recombination. One normal possibility is that it can occur at any time (Figure 1(b), solid blue curve, lower CB), while the other is determined by the symmetry of optical transition, only happens recombination at the  $\Gamma$  point along laser electric field when laser has been propagating half a cycle (Figure 1(b), solid green curve, higher CB), which behaviors like anomalous interband. The recombination instant of two scenarios exhibits significant difference. Recombination only at the  $\Gamma$  point happens later, leading to the temporal delay compared with normal situation, manifesting the asynchronous occupation. Eventually, FWHM of spectrum dominated anomalous interband broadens ( Figure 1(a)).

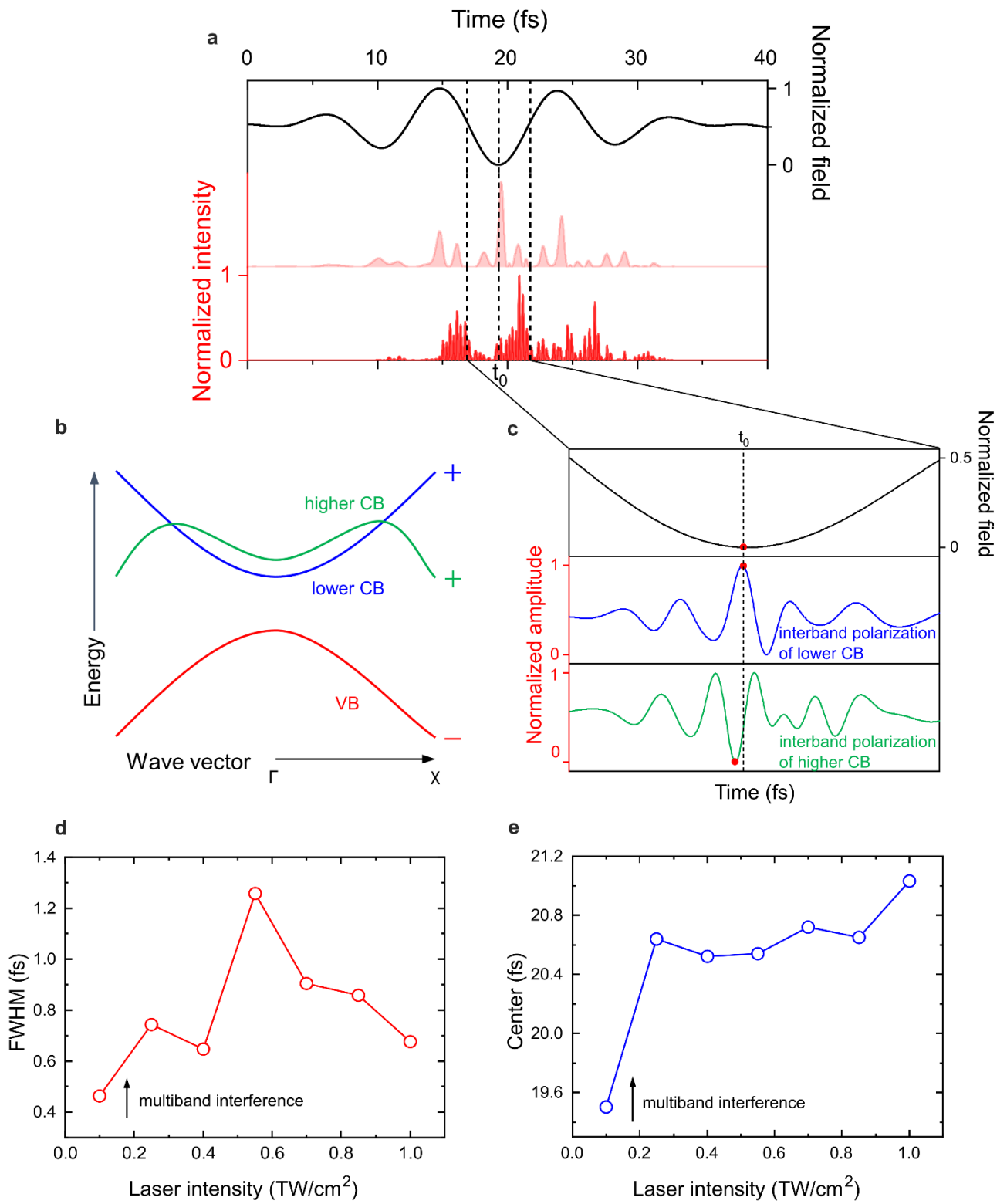


**Figure 1. The anomalous interband emission mechanism.** (a) Temporal characteristic of APT in different laser intensity. The solid black line is the shape of laser electric field, the shallow red line is the APT in lower intensity and the dark red

line is in higher intensity. (b). The illustration of multi-and emission in bandstructure of bulk silicon along laser electric field ( $\Gamma X$ ), where plus and minus sign represent the different symmetry of energy band. (c) Time-domain characteristics of the corresponding emission processes. (d), (e) The center and FWHM of the peak in the low-pass filtered signal up to 4.3eV varies with changes with laser intensity.

## II. METHODS

### A. Calculating HHG, APT from rt-TDDFT

We solve the time-dependent Kohn-Sham equations to obtain the Kohn-Sham orbital  $\Psi_i(\mathbf{r}, t)$  basing on wavefunction expansion by adiabatic eigenstates basis [35]. Here,  $i$  denotes the band index and  $k$  point. The laser potential is considered in velocity gauge:

$$i \frac{\partial}{\partial t} \Psi_i(\mathbf{r}, t) = \left( \frac{1}{2} (-i\nabla + \mathbf{A})^2 + v_{ext}(\mathbf{r}, t) + v_{HF}[n(\mathbf{r}, t)] + v_{xc}[n(\mathbf{r}, t)] \right) \Psi_i(\mathbf{r}, t) \quad (1)$$

where  $v_{ext}$  is the electron-ion potential,  $v_{HF}$  is the Hartree part of the Coulomb electron-electron interaction,  $v_{xc}$  is the exchange-correlation potential,  $\mathbf{A}$  is the laser vector potential, which is simulated in dipole approximation [36]:  $\mathbf{A}(\mathbf{r}, t) \approx \mathbf{A}(t) = A_0 \sin^2(t\pi/\delta) \sin(\omega_0 t)$ , where  $A_0$  is the peak potential,  $\delta$  is the total elapsed time,  $\omega_0$  is the carrier angular frequency, the electric field  $\mathbf{E}$  can be derived from the relationship:  $\mathbf{E}(t) = -\partial \mathbf{A}(t)/\partial t$ .

We can get the time-dependent electron spatial density by  $n(\mathbf{r}, t) = \sum_i |\Psi_i(\mathbf{r}, t)|^2$ . The microscopic current  $\mathbf{j}(\mathbf{r}, t)$  can be computed as:

$$\mathbf{j}(\mathbf{r}, t)_i = \frac{1}{2} (\langle \Psi_i(\mathbf{r}, t) | -i\nabla + \mathbf{A} | \Psi_i(\mathbf{r}, t) \rangle) + c. c. \quad (2)$$

where  $c. c.$  denotes the complex conjugate. The attosecond pulse trains (APT) and corresponding high harmonics generation (HHG) spectrum are obtained from squaring of the modulus and taking the Fourier transform ( $\mathcal{FT}$ ) of the first derivative of time-dependent current:

$$\text{APT}(t) \propto \left| \left\{ \frac{\partial}{\partial t} \int_{\Omega} d^3\mathbf{r} \mathbf{j}_i(\mathbf{r}, t) \right\} \right|^2 \quad (3)$$

$$HHG(\omega) \propto \left| \mathcal{FT} \left\{ \frac{\partial}{\partial t} \int_{\Omega} d^3\mathbf{r} \mathbf{j}_i(\mathbf{r}, t) \right\} \right|^2 \quad (4)$$

where  $\Omega$  is the system volume.

## B. Processing and characterizing signal

The time-frequency analysis is performed by continuous wavelet transform [37]:

$$W(\tau, s) = \left| \frac{1}{\sqrt{s}} \int_{-\infty}^{\infty} dt \left\{ \frac{\partial}{\partial t} \int_{\Omega} d^3\mathbf{r} \mathbf{j}_i(\mathbf{r}, t) \cdot \Phi^* \left( \frac{t - \tau}{s} \right) \right\} \right|^2 \quad (5)$$

where  $\tau, s$  is the translation coefficient and scaling coefficient, respectively.  $\Phi^*(t)$  is the father wavelet function, the corresponding mother wavelet function is complex Morlet wavelet, which is given by:  $\Phi(t) = 1/\sqrt{\pi B} \cdot \exp(-t^2/B) \cdot \exp(j2\pi Ct)$ , where  $B$  is the band width (chosen as 1),  $C$  is the center frequency (chosen by proper parameters) and  $j$  is the imaginary unit. The isolated attosecond pulse (IAP) can be extracted from the coherent superposition of consecutive harmonics [38]:

$$IAP(t) = \left| \sum_{\omega_i}^{\omega_f} e^{i\omega t} \mathcal{FT} \left\{ \frac{\partial}{\partial t'} \int_{\Omega} d^3\mathbf{r} \mathbf{j}_i(\mathbf{r}, t') \right\} \right|^2 \quad (6)$$

where  $\omega_i$  and  $\omega_f$  determine the energy window used for calculating the IAP.

Accounting for the center inversion symmetry of material and laser, only odd order harmonics are obtained. The yield of odd order harmonic is defined as the energy region between adjacent even order harmonics [39]. The yield of  $n$ th harmonics is given by the following equation:

$$I_{HHG}(n) = \int_{(n-1)\omega}^{(n+1)\omega} HHG(\omega') d\omega' \quad (7)$$

where  $\omega'$  is the frequency of the laser carrier.

### III. RESULTS (we use silicon as the example)

#### A. Comparison: Experimental Results (previous work), this work

To validate the reliability of our calculation approach, we reproduce the experimental results of silicon along different laser polarization and photon energy from the literature [40]. A lower intensity  $0.16\text{ TW}/\text{cm}^2$  is employed because of the reflection of surface and underestimated bandgap of DFT [10,39]. The main features of high harmonic generation (HHG) obtained from our TDDFT calculations are essentially consistent with the experimental observations (Figure 2). Also, we note the small discrepancies are due to lack of consideration for dephasing factors and macroscopic propagation effects [20,29,40–42].

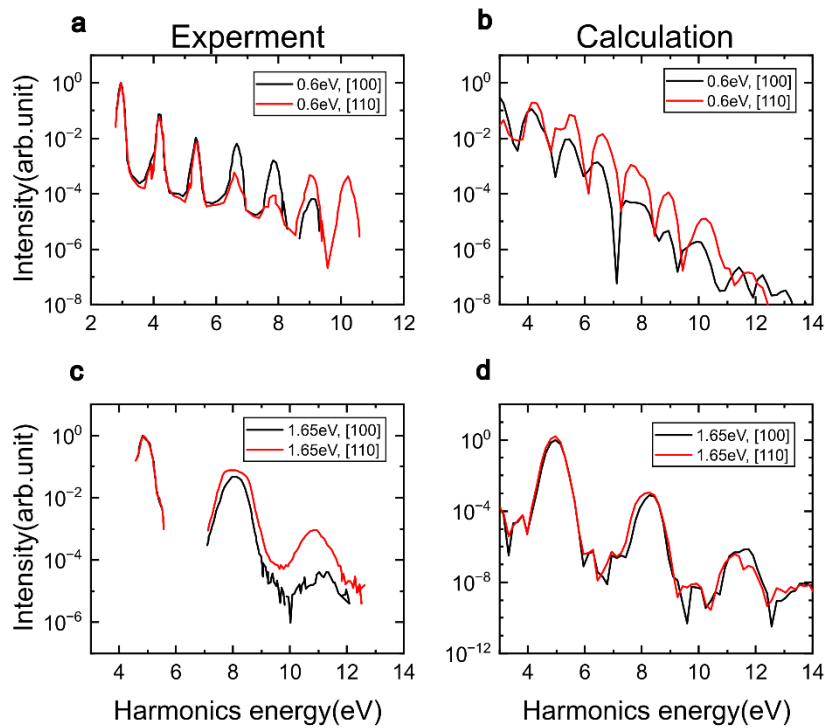


**Figure 2. Experiment v.s. Calculation.** (a) and (c) represent the experimental results of HHG under laser intensities of  $3.00\text{ TW}/\text{cm}^2$  for carrier photon energies of 0.6eV and 1.65eV, including HHG along laser polarization [100] and [110], respectively; (b), (d) represent the corresponding computational results from TDDFT.

## B. Time-Frequency Characteristics of Ultrafast Electron Dynamics

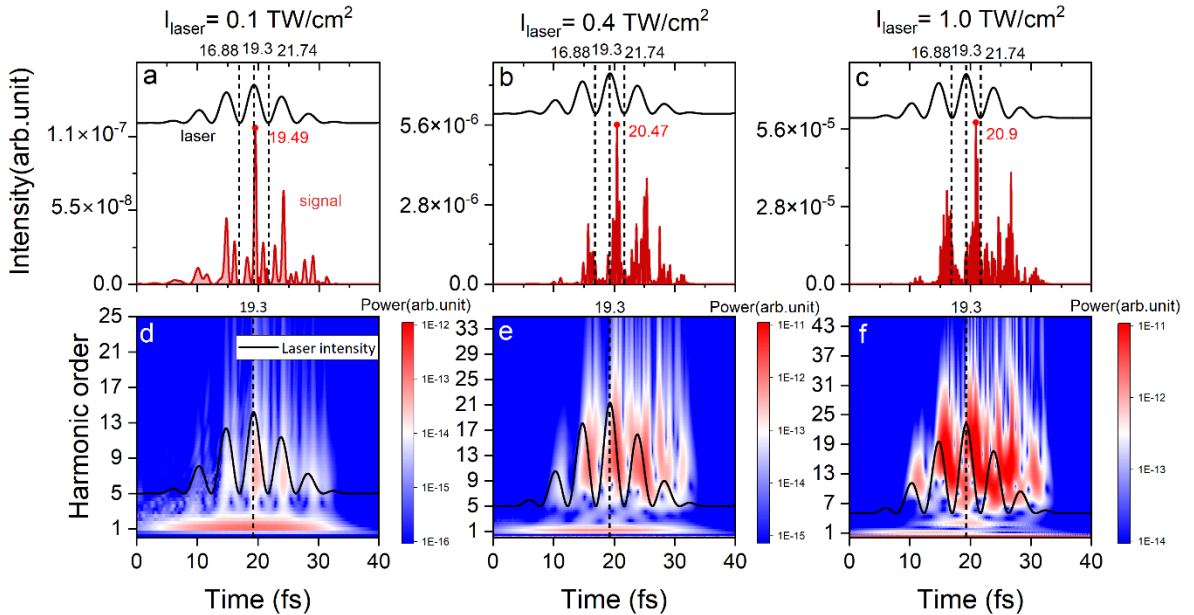


**Figure 3. APT emission and wavelet analysis in different intensity.** (a), (b) and (c) represent the APT emission at  $0.10 \text{ TW/cm}^2$ ,  $0.40 \text{ TW/cm}^2$  and  $1.00 \text{ TW/cm}^2$ , respectively. (c), (d) and (e) show the corresponding time-frequency analysis.

To investigate the role of multi-band on the characteristic of APT emission, we pick three standard sets of progressively increasing laser intensities to compare the involvement of additional energy bands, shown in Figure 3. Figure 3 (a), (b) and (c) depict APT under intensities of  $0.10 \text{ TW/cm}^2$ ,  $0.40 \text{ TW/cm}^2$  and  $1.00 \text{ TW/cm}^2$ , respectively. It's evident that the maximum peak centers of APT (after filtering) emitting photons shift to be later and the signal are becoming noisier as the laser intensity increases (see **APPENDIX B**). This is attributed to the fact that as the intensity increases, more carriers and bands are involved, which leads to the interband progress gradually dominating, causing the emitting instant to shift progressively later than the peak of laser intensity by the interferometry of dipole phase [43]. Further time-frequency analysis confirmed our ideas (Figure 3 (d), (e) and (f)). The lack of chirp observed

in Figure 3a acts indicates that the emission is dominated by intraband mechanisms at low intensity, while the significant chirp observed in Figure 3 (d), (e) suggests that interband mechanisms are the primary drivers[21,23,66]. Additionally, we can see that APT emission of high-frequency part exhibits more significant negative chirp, which is different from previous findings [20,29,41].

## IV. DISCUSSION

### A. The role of temporal multi-band electron occupation in APT emission.

In order to understanding the peculiar changes of FWHM and the shift of the highest peak center, we begin from the derivation of APT in solid-state material basing on the fundamental framework of quantum mechanics in Heisenberg picture, noting that the intermediate results align with the groundbreaking studies [25] and we extend it to a more concrete form (see **APPENDIX C** for more details).

$$\begin{aligned} \text{APT}(t) &\propto \left\{ \int_{\Omega} d^3\mathbf{r} \sum_i n_i(\mathbf{r}, t) \cdot \nabla(v_{ion}(\mathbf{r})) + N_e \mathbf{E}(t) \right\}^2 \\ &\propto \left\{ \int_{\Omega} d^3\mathbf{r} \left( \sum_{l,k} \overline{\partial\mathcal{C}}_{l,k(t)}(t) \cdot \varphi_{l,k(t)}^*(t) \varphi_{l,k(t)}(t) \right) \cdot \nabla v_{ion}(\mathbf{r}) + N_e \mathbf{E}(t) \right\}^2 \end{aligned} \quad (8)$$

Here,  $n_i(\mathbf{r}, t)$  represents the time-dependent electron spatial density, which can be calculated through  $n_i(\mathbf{r}, t) = |\Psi_i(\mathbf{r}, t)|^2$ , where  $i$  is the index of the Kohn-Sham orbital and  $\Psi_i(\mathbf{r}, t)$  is the wavefunction,  $\overline{\partial\mathcal{C}}_{l,k(t)}(t)$  is the time-dependent occupation,  $\varphi_l$  is the adiabatic expansion basis with  $l$  is as the index,  $v_{ion}(\mathbf{r})$  is the static ionic potential,  $N_e$  is the total number of electrons in system  $\Omega$ ,  $\mathbf{E}(t)$  is the laser electric field in dipole approximation,  $\mathbf{A}(t)$  is the corresponding vector potential (which relates to  $\mathbf{E}(t)$  as  $\mathbf{E}(t) = -\partial\mathbf{A}(t)/\partial t$ ).  $\mathcal{FT}$  means Fourier transform. It should be noted that the influence of nuclear motion [44,45], non-adiabatic Coulomb interaction of Hartree part and exchange-correlation functional [25,46], spin polarization [47,48], electron and impurity scattering [49–52] on Hamiltonian extend beyond the scope of this article.

A notable finding is that the time evolution of APT in a given material and laser is profoundly affected by the temporal occupation distribution of different Kohn-Sham orbitals, which could be understood through the fact that the emission source of APT originates from the generated current induced by electron behavior. From the time-domain perspective, While the electric field primarily governs the temporal characteristics of APT (as indicated by the second term in equation (8), second term), this synchronization with the laser field only reflects the intra-band harmonics behavior [12,43]. However, only can the anomalous temporal phenomenon be controlled by the first term of equation(8), which is closely related to the occupation of different orbitals. On the other hand, the frequency-domain, the spectrum of HHG should be dominated by the 1<sup>st</sup> harmonic basing on the Fourier transform of electric field (ignoring the envelope for simplicity). More importantly, what matters most is the nonlinear components, i.e., the first term of equation (9) in **APPENDIX C**. Besides, the larger spatial fluctuation of electron-ion potential and enormous total electron number [18] will enhance the harmonic yield. Also, we can't disregard the possible interference between electric field and high-order term. Thus, firstly, we could find the temporal shift compared with electric field in APT may significantly affect the spatial occupation over time, which is presented through the charge differential density in spatial occupation over time (see **Appendix D** for details), which further leads to the asynchronous distribution of temporal electron density. So, in Figure 5, we present the electron occupation on the primary bands for different laser intensities. At low intensity, the carrier occupation is concentrated in VBM and CBM, remaining synchronized with the changes in electric field (Figure 5 (c), (e), (g)), following a half-cycle variation of laser intensity (proportional to the square of electric field), indicating that intra-band process dominates emission. In stark contrast, at high intensity, a significant portion of carriers are distributed in higher energy bands (Figure 5 ((d), (f), (h))). While the carriers lying on the lower bands (CBM+1 and CBM+3, the occupation of CBM+1 and CBM+3 is exchanged due to the band crossing) still exhibit similar characteristics to low field strength, asynchronous behavior emerges in the higher energy bands. The occupation of CBM+1 lags behind those of electric field, suggesting that the occupation dynamics of multiple main bands directly influence the changes in APT emission at high intensity.

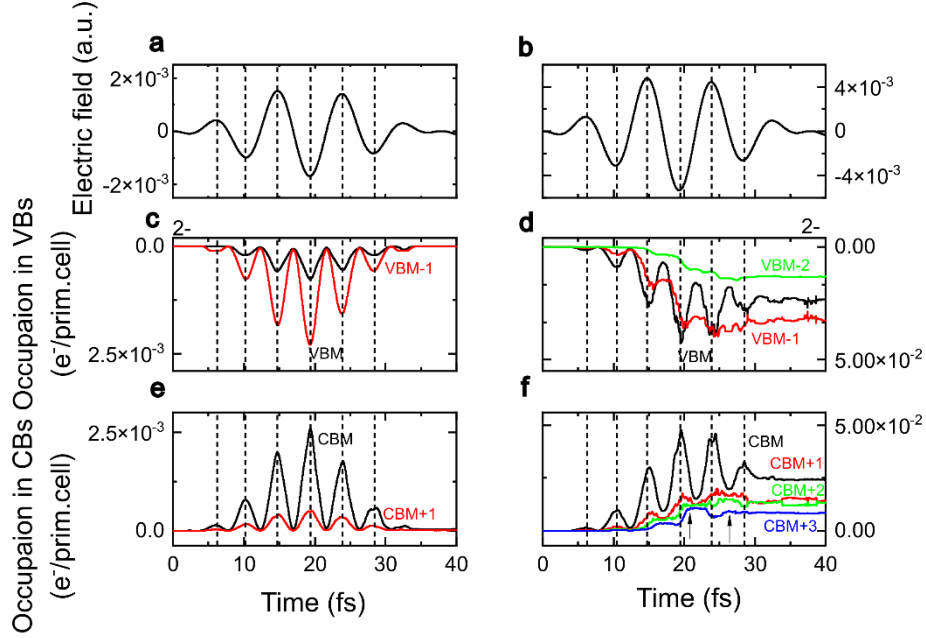


**Figure 4. Temporal evolution of multi-band electron occupation under different laser intensity.** Panels (a), (c), (e) depict electric field, the evolution of electron occupation in valence and conduction bands over time under  $0.10 \text{ TW}/\text{cm}^2$ , while panels (d), (f), (h) represent the corresponding cases of  $1.00 \text{ TW}/\text{cm}^2$ .

## B. Transition dipole moment guided by symmetry.

The anomalous variations observed between different multiband transition sparked our interest. To uncover the underlying mechanisms, we analyze the differences in transition dipole element (TDM) between different multiple bands, which significantly contributes to the interband process [20,42]. Our quantitative analysis reveals that, along the direction of the laser polarization (for simplicity), the TDM primarily exist among VBM, CBM+1 and CBM+3. Specifically, the TDM between VBM and CBM+3 only exist at the  $\Gamma$  point, while the TDM between VBM and CBM+1 are distributed along the  $\Gamma X$  direction (Figure 6(c)). This TDM provides a reasonable explanation for the anomalous occupation behavior: during

the interband process, electrons on CBM+1 can recombine and return to VBM at any position along the  $\Gamma X$  direction (i.e. normal interband process), while electrons lying on CBM+3 can only recombine and return to VBM at the  $\Gamma$  point after half a laser cycle (i.e. anomalous interband process). This difference at recombination instant leads to the observed disparity in occupation. Due to the difficulty of controlling TDM and the limited parameters in TDDFT, we utilize the one-dimension(1D) multi-band semiconductor Bloch equations (SBE) to simulate and qualitatively reproduce the occupation delay successfully (Figure 6(d), see **Appendix E** for calculation details).

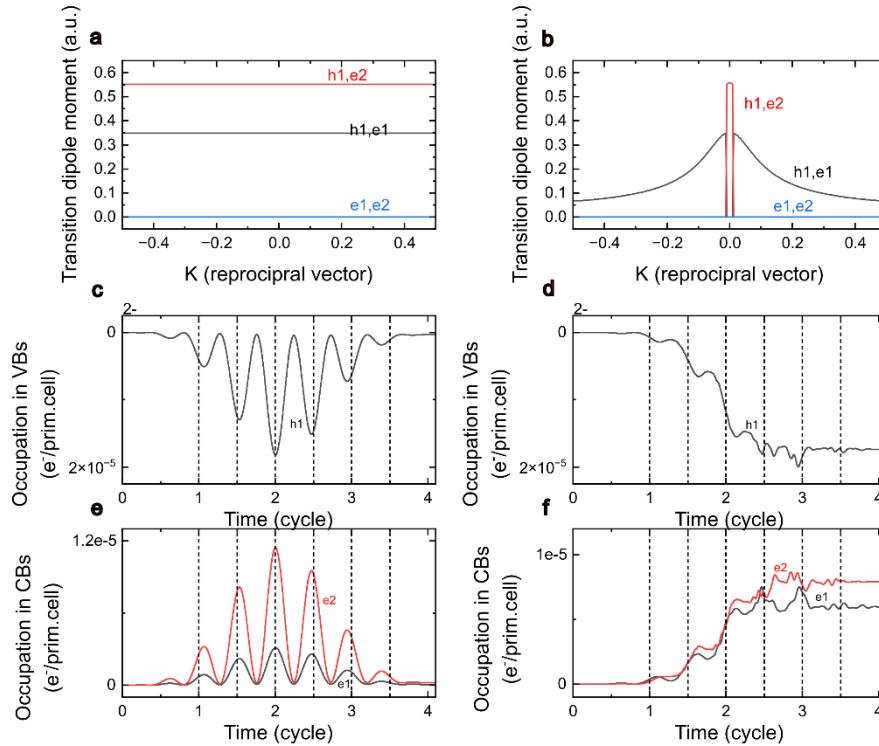


**Figure 5. Simulation of 1D multi-band SBEs simulation.** a, b, transition dipole moment along laser field fixed at  $\Gamma$  point and k-dependent obtained by DFT. c and e are electron occupation of VBM(h1) and hole occupation of CBM (e1, e2), respectively, corresponding to TDM of a. d and f are electron occupation of VBM(h1) and hole occupation of CBM (e1, e2), respectively, corresponding to TDM of b.

Based on the above analysis, we could deliver such aggregated physical picture: Firstly, the temporal APT could be described by the temporal electron occupation. Secondly, at low field, the APT is synchronized with laser field due to the intraband emission. And the synchronization of occupation with laser can could be explained by the Keldysh strong-field theory [53,54], i.e., the excitation carriers are proportional to the laser intensity and the instantaneous bandgap of the material, which can be considered nearly constant at low intensities due to the nearly constant momentum, as described by Bloch's acceleration theorem. While at high field, the participation of multiple bands makes APT emission process more complex. The anomalous interband processes begin to involve, although the peak intensity of APT increases, the FWHM gradually enlarges, and the yield of partial harmonics from the interference between more complex emission ways. As the laser intensity continues to increase, normal interband processes become dominant, leading to a gradual reduction in FWHM.

## **V. CONCLUSION**

In summary, we have elucidated the impact of multi-band effects on APT in solid materials. Our analytical derivation shows APT emission can be characterized by the occupation of multiple bands. Using ab initio calculations, we unveiled that the optical transition (forbidden transition) under symmetry constraints lead to interference in inter-band emission process, resulting in temporal delay and broad FWHM in APT. This delay is reflected in occupation on different bands and we also have provided analytical evidence, which hinders the extraction of IAP and reduce the yield of harmonics. Our work could provide directional guidance to search for suitable material and parameters for solid-state attosecond laser.

## **ACKNOWLEDGEMENTS**

## APPENDIX A: Computational Details of ab initio Method

All static calculations and real-time time-dependent density functional theory (rt-TDDFT) are performed with the ab initio package PWMAT [35,55]. We utilize the optimized norm-conserving pseudopotentials Vanderbilt [56] and adiabatic Perdew-Burke-Ernzerhof (PBE) exchange-correlation functions. The expansion of the evolved wavefunction is based on plane-wave basis with a cutoff energy of 50 Ry, and an  $12 \times 12 \times 12$  k-point mesh with Monkhorst-Pack grids to sample the irreducible Brillouin zone of primitive cell. Si (2s2p2) are considered as valence electrons in simulation.

As is well known, DFT can't avoid to underestimate the band gap of materials due to the limitations in accounting for self-interaction [57] and excitonic effects [58]. However, neglecting this aspect seldom affects our conclusions. Additionally, effects such as spin, dephasing caused by lattice and impurity scattering [25] and carrier lifetime are also disregarded. Furthermore, common nonlinear optical phenomena are not taken into account, like self-focusing and propagation effects.

The primitive cell of bulk silicon with a lattice constant  $a = 5.47\text{\AA}$  is used as the prototype. We employ the sine square envelope with full width at half maximum (FWHM) of 20fs and a center carrier wavelength of 3000 nm (corresponding to 0.43eV) without carrier-envelope phase. The laser of peak intensity ranges from  $0.1 \text{ TW}/\text{cm}^2$  to  $1.0 \text{ TW}/\text{cm}^2$  (in vacuum, ignoring surface reflection), which is polarized along [100] direction.

## APPENDIX B: Low-pass Filtering Signal

To provide a more quantitative analysis of the quality and characteristics of the APT signal under different laser intensity, we applied a low-pass filter to all signals, using the cutoff energy at the lowest intensity, to obtain a clearer signal. The resulting peak intensity and peak center position are shown in the figure below.

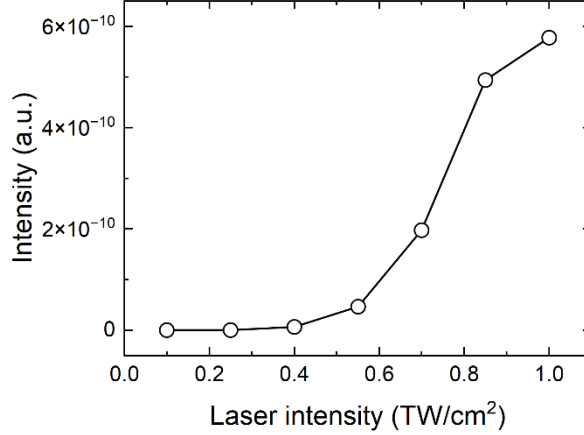


**Figure S 1. Intensity of maximum peak.** Peak intensity after applying low-pass filtering under different laser intensity.

### APPENDIX C: Analytical Derivation of APT and HHG from Adiabatic Basis and Occupation

A couple of years ago, Nicolas Tancogne-Dejean et. al derived the approximate analytical expressions in ab initio calculation for HHG and APT using the language of second quantization [25]. Here, we have derived equivalent result based on the quantum mechanical framework in Heisenberg picture and extend it. For simplicity, we ignore the effect of nuclear motion, non-adiabatic Coulomb interaction of Hartree part and exchange-correlation functional, spin polarization, electron and impurity scattering on Hamiltonian;

The expression for the current in velocity can be written as follows,

$$\begin{aligned}
 \mathbf{j}(\mathbf{r}, t) &= \frac{i}{2} (\Psi(\mathbf{r}, t) \nabla \Psi(\mathbf{r}, t)^* - \Psi(\mathbf{r}, t)^* \nabla \Psi(\mathbf{r}, t)) + \widehat{\mathbf{A}}(\mathbf{r}, t) \cdot \Psi(\mathbf{r}, t) \Psi(\mathbf{r}, t)^* \\
 &= \frac{1}{2} (\langle \Psi(\mathbf{r}, t) | \widehat{\mathbf{p}} + \widehat{\mathbf{A}}(\mathbf{r}, t) | \Psi(\mathbf{r}, t) \rangle + c. c.)
 \end{aligned} \tag{2}$$

where  $\Psi(\mathbf{r}, t)$  is the wave function from solution of Kohn-Sham equation.  $\widehat{\mathbf{A}}(\mathbf{r}, t)$  is the operator of vector potential,  $\widehat{\mathbf{p}}$  is the operator of momentum,  $c. c.$  means the corresponding complex conjugate.

We take  $\widehat{\mathbf{Q}} = \widehat{\mathbf{p}} + \widehat{\mathbf{A}}$ , in velocity, consider the effectiveness of electron interaction and exchange-

correlation term of ground state to Hamiltonian [25] and substituting it into equation (18).

$$\begin{aligned}
\frac{\partial}{\partial t} \langle \hat{\mathbf{p}} + \hat{\mathbf{A}} \rangle &= i \langle \frac{(\hat{\mathbf{p}} + \hat{\mathbf{A}})^2}{2} + v_{eff}(\mathbf{r}), \hat{\mathbf{p}} + \hat{\mathbf{A}} \rangle + \langle \frac{\partial}{\partial t} (\hat{\mathbf{p}} + \hat{\mathbf{A}}) \rangle \\
&= i \langle [v_{eff}(\mathbf{r}), \hat{\mathbf{p}} + \hat{\mathbf{A}}] \rangle + \langle \frac{\partial}{\partial t} (\hat{\mathbf{p}}) \rangle + \langle \frac{\partial}{\partial t} (\hat{\mathbf{A}}) \rangle \\
&= i \langle [v_{eff}(\mathbf{r}), \hat{\mathbf{p}} + \hat{\mathbf{A}}] \rangle + \langle \frac{\partial}{\partial t} (\hat{\mathbf{A}}) \rangle
\end{aligned} \tag{3}$$

where  $v_{eff}(\mathbf{r})$  includes electron-ion Coulomb potential  $v_{ion}(\mathbf{r})$ , electron interaction of Hartree part  $v_{HF}(\mathbf{r})$  and exchange-correlation  $v_{xc}(\mathbf{r})$  of ground state.

The first term can be simplified as follows,

$$i \langle [v_{eff}(\mathbf{r}), \hat{\mathbf{p}} + \hat{\mathbf{A}}] \rangle = i \langle [v_{eff}(\mathbf{r}), \hat{\mathbf{p}}] \rangle = \langle \Psi(\mathbf{r}, t) | v_{eff} \nabla - \nabla v_{eff} | \Psi(\mathbf{r}, t) \rangle = -n(\mathbf{r}, t) \nabla v_{eff}(\mathbf{r}) \tag{4}$$

where  $n(\mathbf{r}, t) = \Psi(\mathbf{r}, t)^* \Psi(\mathbf{r}, t)$  is the temporal electron density in space.

Through the relationship  $\mathbf{E}(\mathbf{r}, t) \approx \mathbf{E}(t) = -\partial \mathbf{A}(t) / \partial t$ , we can obtain the electric field in dipole approximation and the second term can be written as follows.

$$\langle \frac{\partial}{\partial t} (\hat{\mathbf{A}}) \rangle = -\langle \hat{\mathbf{E}}(\mathbf{r}, t) \rangle = -\langle \Psi(\mathbf{r}, t) | \hat{\mathbf{E}}(\mathbf{r}, t) | \Psi(\mathbf{r}, t) \rangle = -n(\mathbf{r}, t) \cdot \mathbf{E}(t) \tag{5}$$

Substituting equations (4) and (5) into equation (3), we obtain

$$\langle \frac{\partial}{\partial t} (\hat{\mathbf{p}} + \hat{\mathbf{A}}) \rangle = -n(\mathbf{r}, t) \cdot (\nabla v_{eff}(\mathbf{r}) + \mathbf{E}(t)) \tag{6}$$

Thus, we derive the expression of APT and HHG,

$$\begin{aligned}
APT(\mathbf{r}, t) &\propto \left| \int_{\Omega} d^3\mathbf{r} \left( \frac{\partial}{\partial t} \mathbf{J}(\mathbf{r}, t) \right) \right|^2 \\
&\propto \left| \int_{\Omega} d^3\mathbf{r} \left( \frac{1}{2} (\langle \Psi(\mathbf{r}, t) | \hat{\mathbf{p}} + \hat{\mathbf{A}}(\mathbf{r}, t) | \Psi(\mathbf{r}, t) \rangle + c.c.) \right) \right|^2 \\
&\propto \left| \int_{\Omega} d^3\mathbf{r} \left\{ -n(\mathbf{r}, t) \cdot (\nabla v_{eff}(\mathbf{r}) + \mathbf{E}(t)) \right\} \right|^2 \\
&\propto \left| \int_{\Omega} d^3\mathbf{r} \left\{ n(\mathbf{r}, t) \nabla v_{eff}(\mathbf{r}) + N_e(t) \right\} \right|^2
\end{aligned} \tag{7}$$

$$HHG(\omega) \propto \left| \mathcal{FT} \left\{ \frac{\partial}{\partial t} \int_{\Omega} d^3\mathbf{r} n(\mathbf{r}, t) \nabla v_{eff}(\mathbf{r}) + N_e \mathbf{E}(t) \right\} \right|^2 \quad (8)$$

Where  $N_e$  is the number of total electrons in system  $\Omega$ ,  $\mathcal{FT}$  means Fourier transform. We could obtain HHG from the corresponding Fourier transform, consider electron interaction of Hartree part and exchange-correlation contributions are from internal forces, so equation (4) and (5) reduces to

$$APT(t) \propto \left| \int_{\Omega} d^3\mathbf{r} n(\mathbf{r}, t) \nabla v_{ion}(\mathbf{r}) + N_e \mathbf{E}(t) \right|^2 \quad (9)$$

$$HHG(\omega) \propto \left| \mathcal{FT} \left\{ \frac{\partial}{\partial t} \int_{\Omega} d^3\mathbf{r} n(\mathbf{r}, t) \nabla v_{ion}(\mathbf{r}) + N_e \mathbf{E}(t) \right\} \right|^2 \quad (10)$$

Noting equation (10) is equal to expression of literature [25], now we further write firstly  $n(\mathbf{r}, t)$  with adiabatic state basis expansion following PWMAT.

$$\begin{aligned} n(\mathbf{r}, t) &= \sum_i n_i(\mathbf{r}, t) \\ &= \sum_i \sum_{\mathbf{k}(t) \in BZ} OCC_{i,\mathbf{k}(t)} \Psi_{i,\mathbf{k}(t)}^*(\mathbf{r}, t) \Psi_{i,\mathbf{k}(t)}(\mathbf{r}, t) \\ &= \sum_i \sum_{\mathbf{k}(t) \in BZ} OCC_{i,\mathbf{k}(t)} \sum_l C_{i,l}^*(t) C_{i,l}(t) \varphi_{l,\mathbf{k}(t)}^*(t) \varphi_{l,\mathbf{k}(t)}(t) \\ &= \sum_i \sum_{\mathbf{k}(t) \in BZ} OCC_{i,\mathbf{k}(t)} \sum_{l,\mathbf{k}(t) \in BZ} \{C_{i,l}^*(t) C_{i,l}(t)\} (\varphi_{l,\mathbf{k}(t)}^*(t) \varphi_{l,\mathbf{k}(t)}(t)) \\ &= \sum_{l,\mathbf{k}} \overline{OCC}_{l,\mathbf{k}(t)}(t) \cdot \varphi_{l,\mathbf{k}(t)}^*(t) \varphi_{l,\mathbf{k}(t)}(t) \end{aligned} \quad (11)$$

Where  $n_i(\mathbf{r}, t)$  is the time-dependent electron spatial density which can be calculated through  $n(\mathbf{r}, t) = |\Psi_i(\mathbf{r}, t)|^2$ ,  $i$  is the index of the Kohn-Sham orbital,  $\Psi_i(\mathbf{r}, t)$  is the wavefunction,  $OCC_{i,\mathbf{k}(t)}$  is the static electron occupation,  $\overline{OCC}_{l,\mathbf{k}(t)}(t)$  is time-dependent electron occupation,  $\varphi_l$  is the adiabatic expansion basis,  $l$  is the index of adiabatic basis.

At last, we substitute equation (11) into equations (9), (10) and obtain the final expression;

$$\begin{aligned}
APT(t) &\propto \left| \int_{\Omega} d^3\mathbf{r} \sum_i n_i(\mathbf{r}, t) \nabla(v_{ion}(\mathbf{r})) + N_e \mathbf{E}(t) \right|^2 \\
&\propto \left| \int_{\Omega} d^3\mathbf{r} \left( \sum_{l,k} \overline{\mathcal{OCC}}_{l,k(t)}(t) \cdot \varphi_{l,k(t)}^*(t) \varphi_{l,k(t)}(t) \right) \cdot \nabla v_{ion}(\mathbf{r}) + N_e \mathbf{E}(t) \right|^2
\end{aligned} \tag{12}$$

$$HHG(\omega) \propto \left| \mathcal{FT} \left\{ \int_{\Omega} d^3\mathbf{r} \left( \sum_{l,k} \overline{\mathcal{OCC}}_{l,k(t)}(t) \cdot \varphi_{l,k(t)}^*(t) \varphi_{l,k(t)}(t) \right) \cdot \nabla v_{ion}(\mathbf{r}) + N_e \mathbf{E}(t) \right\} \right|^2 \tag{13}$$

From the equations above, we can find the temporal occupation of carriers  $\left(\overline{\mathcal{OCC}}_{l,k(t)}(t)\right)$  have an obvious impact on the temporal characteristic of APT and HHG.

#### Appendix D: Temporal Delay of Differential Charge Density under Different Laser Intensity

We depict the material's representation in real space, laser field direction  $[1\bar{1}1]$  and plane (121) in Figure S 2, to present the differential charge density between the instant ranging from  $t = 19.0fs \sim 20.0fs$  (corresponding to the area of strongest intensity of laser) and  $t_0 = 0fs$  in the plane (121) (which is parallel to laser field) for  $0.10 TW/cm^2$  and  $1.00 TW/cm^2$  in [attachment](#), respectively. It can be observed that, firstly, under  $1.00 TW/cm^2$ , the excited carriers are more pronounced. Secondly, the distribution of excited carriers in space under  $0.10 TW/cm^2$  symmetrically changes around the laser peak (about 19.4fs), indicating a normal variation. However, under  $1.00 TW/cm^2$ , i.e. multi-band, there is a noticeable temporal delay phenomenon. Most obviously, the peak excited occupation in differential charge density happens at  $t = 19.4fs$  for  $0.10 TW/cm^2$ , while it occurs at  $t = 19.5fs$  for  $1.00 TW/cm^2$ . Finally, we could find the different temporal trends in different intensities.

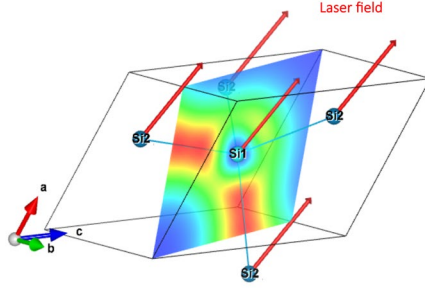


Figure S 2. Primitive cell of silicon, laser electric field and plane (121).

## APPENDIX E: 1D multi-band semiconductor Bloch equations

We numerically solve one-dimensional multi-band semiconductor Bloch equations to validate the occupation delay phenomenon obtained from ab initio calculation. Tight-banding model is utilized to fit the bandstructure calculated from the software “PVMAT” [59] with cosine function, also the transition dipole moment (TDM)  $\mu_k^{\lambda\lambda'}$  between  $\Gamma$  point and others is obtained from this package, where  $\lambda, \lambda'$  is the band index,  $k$  is the wave vector of 1D Brillouin zone along  $\Gamma X$  direction. We extend TDM between  $\Gamma$  point and others to all points of 1D Brillouin zone with  $k \cdot p$  perturbative theory [20,28,29]. In the solution, compared with the results in TDDFT in 3D, a weaker intensity  $0.015 TW/cm^2$  is used, crucial bands including one valence band ( $h = band4$ ) and two conduction bands ( $e = band6,8$ ) are utilized, where we preform it in the following way;

$$i\hbar \frac{\partial}{\partial t} p_k^{he} = \left( \varepsilon_k^h + \varepsilon_k^e - i \frac{\hbar}{T_2} \right) p_k^{he} - \Omega_k^{eh}(t)(1 - f_k^h - f_k^e) + i|e|\mathbf{E}(t)\nabla_k p_k^{he} + \sum_{\lambda} (\Omega_k^{\lambda h} p_k^{\lambda e} - \Omega_k^{e\lambda} p_k^{h\lambda}) \quad (14)$$

$$i\hbar \frac{\partial}{\partial t} p_k^{ee'} = \left( \varepsilon_k^{e'} - \varepsilon_k^e - i \frac{\hbar}{T_2} \right) p_k^{ee'} + \Omega_k^{e'e}(t)(f_k^{e'} - f_k^e) + i|e|\mathbf{E}(t)\nabla_k p_k^{ee'} + \sum_{\lambda} (\Omega_k^{\lambda e} p_k^{\lambda e'} - \Omega_k^{e'\lambda} p_k^{e\lambda}) \quad (15)$$

$$i\hbar \frac{\partial}{\partial t} p_k^{hh'} = \left( \varepsilon_k^h - \varepsilon_k^{h'} - i \frac{\hbar}{T_2} \right) p_k^{hh'} + \Omega_k^{hh'}(t)(1 - f_k^h - f_k^{h'}) + i|e|\mathbf{E}(t)\nabla_k p_k^{hh'} + \sum_{\lambda} (\Omega_k^{\lambda h} p_k^{\lambda h'} - \Omega_k^{h'\lambda} p_k^{h\lambda}) \quad (16)$$

$$\hbar \frac{\partial}{\partial t} f_k^h = -2Im \left[ \sum_{\lambda} (\mathbf{\Omega}_k^{\lambda h} (p_k^{h\lambda})^*) \right] + |e| \mathbf{E}(t) \nabla_k f_k^h \quad (17)$$

$$\hbar \frac{\partial}{\partial t} f_k^e = -2Im \left[ \sum_{\lambda} (\mathbf{\Omega}_k^{e\lambda} (p_k^{e\lambda})^*) \right] + |e| \mathbf{E}(t) \nabla_k f_k^e \quad (18)$$

Here,  $p_k^{he}$ ,  $p_k^{ee'}$ ,  $p_k^{hh'}$  is the interband polarization of different kind,  $f_k^e$ ,  $f_k^h$  represent the time-dependent electron and hole population of corresponding band, respectively,  $\varepsilon_k^e = E_k^e$ ,  $\varepsilon_k^h = -E_k^h$  represent the single particle energies of corresponding band omitting renormalization,  $\mathbf{\Omega}_k^{\lambda\lambda'}(t) = \mu_k^{\lambda\lambda'} \mathbf{E}(t)$  is the Rabi frequency without renormalization. Besides, we also ignore the long lifetime of carriers, high order particle correlations such as biexcitons [60]. In our simulation, constant dephasing time  $T_2 = 484as$  and time evolution step  $dt = 10as$  are employed. The macroscopic polarization is given by;

$$P(t) = \sum_{\lambda,\lambda',k} \mu_k^{\lambda\lambda'} p_k^{\lambda\lambda'}(t) \quad (19)$$

We could obtain the intra-band current from the band group dispersion profile and band occupation;

$$J(t) = \sum_{h,k} \frac{|e|}{\hbar} (\nabla_k E_k^h) f_k^h(t) + \sum_{e,k} \frac{|e|}{\hbar} (\nabla_k E_k^e) f_k^e(t) \quad (20)$$

Finally, the total harmonics emission is given by as follows in acceleration form of HHG which is convenient to compare with results from TDDFT;

$$APT(t) \propto \left| \frac{\partial}{\partial t} \left( \frac{\partial P_t}{\partial t} + J(t) \right) \right|^2 \quad (21)$$

## Appendix F. Signature of non-perturbative optical emission under strong field

Figure S 3 shows the strong field process in different intensities. In Figure S 3 (a), The dashed black line is the fit of data in perturbative regime for 3<sup>rd</sup> harmonic generation. The solid blue dotted line is the

3<sup>rd</sup> harmonic intensity dependence of laser strength. It illustrates that it's in non-perturbative regime. In Figure S 3 (b), we plot the laser intensity dependence of excited carriers, annotating the Keldysh parameters  $\gamma = \omega_0 \sqrt{|m_{e-h}|E_g}/eE_0$ , and find the dominant excitation in tunneling regime, where  $\omega_0$  is the center frequency of laser,  $m_{e-h} = m_e m_h / (m_e + m_h)$  is the reduced effective mass along electric field of electron and hole,  $E_g$  is the band gap,  $E_0$  is the electric field strength. In our ab initio calculation,  $\omega_0$  is equal to 0.0158a.u.,  $m_e$  and  $m_h$  is equal to  $-0.466m_0$  and  $-0.273m_0$  (from PWMAT), respectively. Considering the strong field ionization occurs mainly at  $\Gamma$  point [10], we roughly take the bandgap at  $\Gamma$  point as  $E_g$ , i.e. 0.0936a.u..

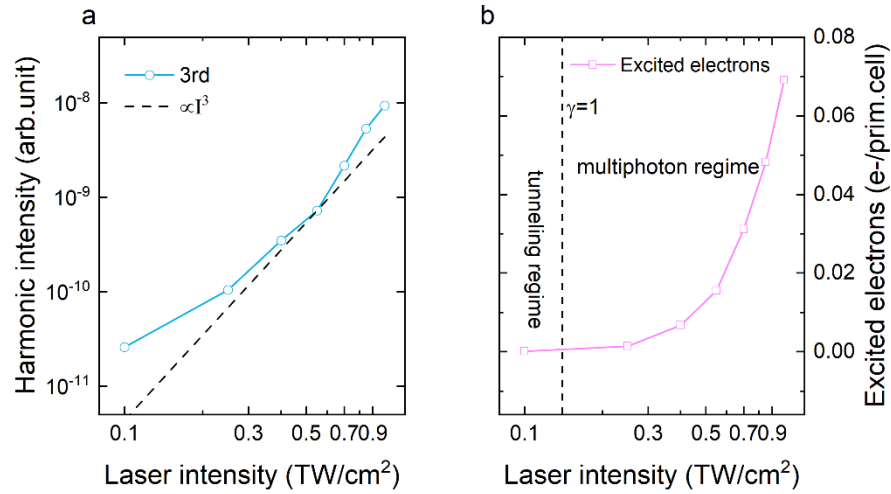


**Figure S 3. Strong field ionization process in different intensities.** (a), the laser field strength dependence of 3rd harmonic and fitted 3rd perturbative harmonic intensity. (b), the laser field strength dependence of excited electrons.

## REFERENCE

- [1] P. M. Paul, E. S. Toma, P. Breger, G. Mullot, F. Augé, Ph. Balcou, H. G. Muller, and P. Agostini, Observation of a Train of Attosecond Pulses from High Harmonic Generation, *Science* **292**, 1689 (2001).
- [2] F. Krausz and M. I. Stockman, Attosecond metrology: from electron capture to future signal processing, *Nature Photon* **8**, 205 (2014).

- [3] N. Dudovich, O. Smirnova, J. Levesque, Y. Mairesse, M. Y. Ivanov, D. M. Villeneuve, and P. B. Corkum, Measuring and controlling the birth of attosecond XUV pulses, *Nature Phys* **2**, 781 (2006).
- [4] P. B. Corkum, Plasma perspective on strong field multiphoton ionization, *Physical Review Letters* **71**, 13 (1993).
- [5] M. Lewenstein, P. Balcou, M. Y. Ivanov, A. L’Huillier, and P. B. Corkum, Theory of high-harmonic generation by low-frequency laser fields, *Physical Review A* **49**, 3 (1994).
- [6] D. Castelvetti and K. Sanderson, Physicists who built ultrafast ‘attosecond’ lasers win Nobel Prize, *Nature* **622**, 225 (2023).
- [7] M. Ferray, A. L’Huillier, X. F. Li, L. A. Lompre, G. Mainfray, and C. Manus, Multiple-harmonic conversion of 1064 nm radiation in rare gases, *J. Phys. B: At. Mol. Opt. Phys.* **21**, L31 (1988).
- [8] S. Ghimire, A. D. DiChiara, E. Sistrunk, P. Agostini, L. F. DiMauro, and D. A. Reis, Observation of high-order harmonic generation in a bulk crystal, *Nature Physics* **7**, 138 (2011).
- [9] M. Hohenleutner, F. Langer, O. Schubert, M. Knorr, U. Huttner, S. W. Koch, M. Kira, and R. Huber, Real-time observation of interfering crystal electrons in high-harmonic generation, *Nature* **523**, 7562 (2015).
- [10] G. Vampa, T. J. Hammond, N. Thir’e, B. E. Schmidt, F. L’egar’e, D. D. Klug, and P. B. Corkum, Generation of high harmonics from silicon, *arXiv: Optics* (2016).
- [11] G. Ndabashimiye, S. Ghimire, M. Wu, D. A. Browne, K. J. Schafer, M. B. Gaarde, and D. A. Reis, Solid-state harmonics beyond the atomic limit, *Nature* **534**, 520 (2016).
- [12] M. Garg, M. Zhan, T. T. Luu, H. Lakhotia, T. Klostermann, A. Guggenmos, and E. Goulielmakis, Multi-petahertz electronic metrology, *Nature* **538**, 7625 (2016).
- [13] Y. S. You, David, and S. Ghimire, Anisotropic high-harmonic generation in bulk crystals, *Nat Phys* **13**, 4 (2017).
- [14] Y. Murakami, M. Eckstein, and P. Werner, High-Harmonic Generation in Mott Insulators, *Physical Review Letters* **121**, 5 (2018).
- [15] N. Tancogne-Dejean and A. Rubio, Atomic-like high-harmonic generation from two-

dimensional materials, *Sci Adv* **4**, 2 (2018).

[16]S. Ghimire and D. A. Reis, High-harmonic generation from solids, *Nature Physics* **15**, 1 (2019).

[17]E. Goulielmakis and T. Brabec, High harmonic generation in condensed matter, *Nature Photonics* **16**, 6 (2022).

[18]J. Park, A. Subramani, S. Kim, and M. F. Ciappina, Recent trends in high-order harmonic generation in solids, *Advances in Physics: X* **7**, 1 (2022).

[19]T. T. Luu, M. Garg, S. Y. Kruchinin, A. Moulet, M. T. Hassan, and E. Goulielmakis, Extreme ultraviolet high-harmonic spectroscopy of solids, *Nature* **521**, 7553 (2015).

[20]G. Vampa, C. R. McDonald, G. Orlando, D. D. Klug, P. B. Corkum, and T. Brabec, Theoretical Analysis of High-Harmonic Generation in Solids, *Physical Review Letters* **113**, 7 (2014).

[21]G. Vampa, T. J. Hammond, N. Thiré, B. E. Schmidt, F. Légaré, C. R. McDonald, T. Brabec, and P. B. Corkum, Linking high harmonics from gases and solids, *Nature* **522**, 7557 (2015).

[22]Y. W. Kim, T.-J. Shao, H. Kim, S. Han, S. Kim, M. Ciappina, X.-B. Bian, and S.-W. Kim, Spectral Interference in High Harmonic Generation from Solids, *ACS Photonics* **6**, 4 (2019).

[23]T. Ikemachi, Y. Shinohara, T. Sato, J. Yumoto, M. Kuwata-Gonokami, and K. L. Ishikawa, Trajectory analysis of high-order-harmonic generation from periodic crystals, *Physical Review A* **95**, 4 (2017).

[24]A. J. Uzan et al., Attosecond spectral singularities in solid-state high-harmonic generation, *Nat. Photonics* **14**, 3 (2020).

[25]N. Tancogne-Dejean, O. D. Mucke, F. X. Kartner, and A. Rubio, Impact of the Electronic Band Structure in High-Harmonic Generation Spectra of Solids, *Phys Rev Lett* **118**, 8 (2017).

[26]G. Orenstein, A. J. Uzan, S. Gadasi, T. Arusi-Parpar, M. Krüger, R. Cireasa, B. D. Bruner, and N. Dudovich, Shaping electron-hole trajectories for solid-state high harmonic generation control, *Opt. Express*, *OE* **27**, 37835 (2019).

[27]Z. Nourbakhsh, N. Tancogne-Dejean, H. Merdji, and A. Rubio, High Harmonics and Isolated Attosecond Pulses from MgO, *Physical Review Applied* **15**, 1 (2021).

- [28]C. R. McDonald, G. Vampa, P. B. Corkum, and T. Brabec, Interband Bloch oscillation mechanism for high-harmonic generation in semiconductor crystals, *Physical Review A* **92**, 3 (2015).
- [29]G. Vampa, C. R. McDonald, G. Orlando, P. B. Corkum, and T. Brabec, Semiclassical analysis of high harmonic generation in bulk crystals, *Phys Rev B* **91**, 6 (2015).
- [30]M. Wu, S. Ghimire, D. A. Reis, K. J. Schafer, and M. B. Gaarde, High-harmonic generation from Bloch electrons in solids, *Physical Review A* **91**, 4 (2015).
- [31]L. Yue and M. B. Gaarde, Imperfect Recollisions in High-Harmonic Generation in Solids, *Phys. Rev. Lett.* **124**, 153204 (2020).
- [32]L. Li, P. Lan, X. Zhu, T. Huang, Q. Zhang, M. Lein, and P. Lu, Reciprocal-Space-Trajectory Perspective on High-Harmonic Generation in Solids, *Physical Review Letters* **122**, 19 (2019).
- [33]C. Yu, S. Jiang, T. Wu, G. Yuan, Z. Wang, C. Jin, and R. Lu, Two-dimensional imaging of energy bands from crystal orientation dependent higher-order harmonic spectra in h-BN, *Phys Rev B* **98**, 8 (2018).
- [34]L. Yue et al., Signatures of Multiband Effects in High-Harmonic Generation in Monolayer MoS<sub>2</sub>, *Physical Review Letters* **129**, 14 (2022).
- [35]Z. Wang, S.-S. Li, and L.-W. Wang, Efficient Real-Time Time-Dependent Density Functional Theory Method and its Application to a Collision of an Ion with a 2D Material, *Physical Review Letters* **114**, 6 (2015).
- [36]O. Neufeld, N. Tancogne-Dejean, U. De Giovannini, H. Hubener, and A. Rubio, Light-Driven Extremely Nonlinear Bulk Photogalvanic Currents, *Phys Rev Lett* **127**, 12 (2021).
- [37]G. R. Lee, R. Gommers, F. Waselewski, K. Wohlfahrt, and A. O’Leary, PyWavelets: A Python package for wavelet analysis, *Journal of Open Source Software* **4**, 1237 (2019).
- [38]M. Chini, K. Zhao, and Z. Chang, The generation, characterization and applications of broadband isolated attosecond pulses, *Nature Photonics* **8**, 3 (2014).
- [39]N. Tancogne-Dejean, O. D. Mücke, F. X. Kärtner, and A. Rubio, Ellipticity dependence of high-harmonic generation in solids originating from coupled intraband and interband dynamics, *Nature*

Communications **8**, 1 (2017).

[40]P. Suthar, F. Trojánek, P. Malý, T. J.-Y. Derrien, and M. Kozák, Role of Van Hove singularities and effective mass anisotropy in polarization-resolved high harmonic spectroscopy of silicon, *Commun Phys* **5**, 1 (2022).

[41]I. Floss, C. Lemell, G. Wachter, V. Smejkal, S. A. Sato, X.-M. Tong, K. Yabana, and J. Burgdörfer, Ab initio multiscale simulation of high-order harmonic generation in solids, *Phys Rev A* **97**, 1 (2018).

[42]S. Jiang, J. Chen, H. Wei, C. Yu, R. Lu, and C. D. Lin, Role of the Transition Dipole Amplitude and Phase on the Generation of Odd and Even High-Order Harmonics in Crystals, *Phys. Rev. Lett.* **120**, 253201 (2018).

[43]J. Lu, E. F. Cunningham, Y. S. You, D. A. Reis, and S. Ghimire, Interferometry of dipole phase in high harmonics from solids, *Nature Photon* **13**, 2 (2019).

[44]L. Li et al., Dynamic Core Polarization in High Harmonic Generation from Solids: The Example of MgO Crystals, *Physical Review Letters* **126**, 18 (2021).

[45]O. Neufeld, J. Zhang, U. De Giovannini, H. Hübener, and A. Rubio, Probing phonon dynamics with multidimensional high harmonic carrier-envelope-phase spectroscopy, *Proceedings of the National Academy of Sciences* **119**, e2204219119 (2022).

[46]H. L. Xiao-Shuang Kong<sup>1</sup>, Symmetry analyses of high-order harmonic generation in monolayer hexagonal boron nitride, *Journal of Physics B: Atomic, Molecular and Optical Physics* (2021).

[47]G. P. Zhang, M. S. Si, M. Murakami, Y. H. Bai, and T. F. George, Generating high-order optical and spin harmonics from ferromagnetic monolayers, *Nat Commun* **9**, 3031 (2018).

[48]M. S. Mrudul, N. Tancogne-Dejean, A. Rubio, and G. Dixit, High-harmonic generation from spin-polarised defects in solids, *Npj Computational Materials* **6**, 1 (2020).

[49]A. Mondal, O. Neufeld, Z. Yin, Z. Nourbakhsh, V. Svoboda, A. Rubio, N. Tancogne-Dejean, and H. J. Wörner, High-harmonic spectroscopy of low-energy electron-scattering dynamics in liquids, *Nat. Phys.* **1** (2023).

- [50]V. E. Nefedova et al., Enhanced extreme ultraviolet high-harmonic generation from chromium-doped magnesium oxide, *Applied Physics Letters* **118**, 20 (2021).
- [51]Y. Zhang, W. He, L. Li, H. Cui, S. Qiao, P. Lan, and P. Lu, Role of localized electronic states in high-order harmonic generation from doped semiconductors, *Phys. Rev. B* **109**, 165204 (2024).
- [52]C. Yu, K. K. Hansen, and L. B. Madsen, Enhanced high-order harmonic generation in donor-doped band-gap materials, *Phys Rev A* **99**, 1 (2019).
- [53]L. V. Keldysh, Ionization in the field of a strong electromagnetic wave, *Sov. Phys. JETP* **20**, 1307 (1965).
- [54]P. Balling and J. Schou, Femtosecond-laser ablation dynamics of dielectrics: basics and applications for thin films, *Rep. Prog. Phys.* **76**, 036502 (2013).
- [55]W. Jia, Z. Cao, L. Wang, J. Fu, X. Chi, W. Gao, and L.-W. Wang, The analysis of a plane wave pseudopotential density functional theory code on a GPU machine, *Computer Physics Communications* **184**, 9 (2013).
- [56]D. R. Hamann, Optimized norm-conserving Vanderbilt pseudopotentials, *Phys. Rev. B* **88**, 085117 (2013).
- [57]J. P. Perdew and A. Zunger, Self-interaction correction to density-functional approximations for many-electron systems, *Phys. Rev. B* **23**, 5048 (1981).
- [58]G. Onida, L. Reining, and A. Rubio, Electronic excitations: density-functional versus many-body Green's-function approaches, *Rev. Mod. Phys.* **74**, 601 (2002).
- [59]C. Yu, X. Zhang, S. Jiang, X. Cao, G. Yuan, T. Wu, L. Bai, and R. Lu, Dependence of high-order-harmonic generation on dipole moment in SiO<sub>2</sub> crystals, *Physical Review A* **94**, 1 (2016).
- [60]F. Langer et al., Lightwave-driven quasiparticle collisions on a subcycle timescale, *Nature* **533**, 7602 (2016).